VNU Journal of Science: Mathematics - Physics

Journal homepage: https://js.vnu.edu.vn/MaP

Original Article

Determination of Defects in Planar $CH_3NH_3PbI_3$ Perovskite Solar Cells Using a SCAPS-1D Simulation Tool

Nguyen Duc Cuong*, Vu Thi Thao, Nguyen Tuan Canh, Nguyen Phuong Hoai Nam, Nguyen Nang Dinh

VNU University of Engineering and Technology, *144 Xuan Thuy, Cau Giay, Hanoi, Vietnam*

Received 29 August 2022
Revised 03 November 2022; Accepted 07 December 2022

Abstract: In this work, electrical simulations of planar $CH_3NH_3PbI_3$ solar cells using a SCAPS-1D (a Solar Cell Capacitance Simulator) simulation tool were performed to determine the density of defects based on the performance parameters and *J-V* characteristics of actual experimental planar $CH_3NH_3PbI_3$ solar cells. Two types of defects (bulk and interface) were introduced into the simulation model. The densities of those defects were found by fitting the *J-V* characteristics and performance parameters including V_{OC}, J_{SC}, and FF to the experimental data. The methods and results reported in this paper showed a close relationship between the parameters of defects in planar perovskite solar cells.

Keywords: Planar solar cells, $CH_3NH_3PbI_3$ perovskite, electrical simulations, defects.

1. Introduction

In recent years, perovskite solar cells (PSCs) have exhibited a rapid rise in power conversion efficiency (PCE) in comparison with other solar cells (SCs) generations including Si SCs. Although PSCs have reached a vulue of the certified PCE as large as 25.5% in 2021 [1], several factors still exist that limit the performance of PSCs. Among those factors, defects contribute mostly to the deterioration in the performance of perovskite solar cells. Defects in PSCs can affect charge transport and the recombination of photo-generated carriers. It was reported that there are several types of bulk defects within the $CH_3NH_3PbI_3$ ($MAPbI_3$, where MA stands for methylammonium (CH_3NH_3)) active layer. Theoretical calculations have shown that dominant intrinsic point defects in $MAPbI_3$ are shallow defects

* Corresponding author.
E-mail address: cuongnd@vnu.edu.vn

https//doi.org/10.25073/2588-1124/vnumap.4771

due to their low formation energies and those shallow acceptors (donors) are responsible for *p*-type (*n*-type) doping [2-4]. Several point defects can be formed under various conditions, including vacancies (V_{MA}', V_{Pb}, and $V_I^{\bullet}$ stand for vacancies of methylammonium, lead, and iodine), interstitials (MA_i, Pb_i, and I_i), cation substitutions (MA_{Pb} and Pb_{MA}), and antisite substitutions (MA_I, Pb_I, I_{MA}, and I_{Pb}). Antisites were predicted to be unstable both energetically and kinetically, so they should spontaneously split into the respective interstitials and vacancies [5]. Among native point defects studied in [6], due to lower formation energy, $V_I^{\bullet}$ and V_{MA}' are much more stable and more abundant than MA_i and I_i, respectively. Negatively charged vacancies (V_{MA}') could result in *p*-type doping, whereas positively charged I vacancy ($V_I^{\bullet}$) results in *n*-type doping, which has been predicted by theoretical calculations [3, 4], and verified experimentally in a study of composition-dependent self-doping behavior in $MAPbI_3$ [7]. In addition to bulk defects, interfacial defects at the interfaces between the active layer (AL) and electron/hole transport layers (ETL/HTL) also affect the performance of devices. The characteristics of two types of defects will be described in more detail in Section 3 (Simulation model).

This work aims to find some parameters used in the SCAPS-1D (a Solar Cell Capacitance Simulator) simulations to obtain results that are in good agreement with the experimental data in terms of V_{OC}, J_{SC}, and *FF* and the current density-voltage (*J*-*V*) curve. These simulation techniques will serve to determine the characteristics of defects within the perovskite active layer (AL) and at the HTL/AL and ETL/AL interfaces as well.

2. Experimental

2.1. Materials

Lead (II) iodide powder (PbI_2, 99%), *N*,*N*-dimethylformamide (DMF), γ-Butyrolactone (GBL), dimethyl sulfoxide (DMSO), anhydrous toluene, chlorobenzene, 1,2-dichlorobenzene, isopropyl alcohol, and acetone were purchased from Sigma-Aldrich. Methylammonium iodide (MAI) was purchased from Greatcell Solar Materials. Poly(3,4-ethylenedioxythiophene)-poly(styrenesulfonate) (PEDOT:PSS, CLEVIOS P VP AI 4083) was purchased from Heraeus Epurio. Phenyl-C61-butyric acid methyl ester (PCBM) was purchased from Nano-C.

2.2. Thin Film and Device Fabrication

The Indium Tin Oxide (ITO)-coated glass (9 Ω sq^{-1}) substrates were patterned and cleaned by successive ultrasonic treatment in acetone, isopropanol, and deionized (DI) water before drying under nitrogen flow. Right before the deposition of the hole-extraction layer (HEL), the ITO-coated glass substrates were treated by plasma for 1 min with 10 sccm of O_2 and Ar, respectively, at a pressure of 25 m Torr and a power of 50 W.

PEDOT:PSS was filtered through a 0.45 μm Polyvinylidene fluoride (PVDF) filter before spin-casting at 3,000 rpm on patterned ITO-coated glass substrates for 60 seconds, followed by annealing at 150 °C for 20 min in air, to yield ~ 40 nm-thick film.

PbI_2 and MAI were dissolved in a mixture solvent of DMF and DMSO (4:1 v/v) or GBL and DMSO (7:3 v/v) at a concentration of 1.0 M under stirring at 60 °C for 12 h. The resulting solution was coated onto the PEDOT:PSS/ITO substrates by a consecutive two-step spin-coating process at 1,000 and 5,000 rpm for 10 and 20 s, respectively. During the second spin-coating step, the substrate (3 cm × 3 cm) was treated with toluene drop-casting within 2-4 seconds after starting this step. The substrate was dried on a hot plate at 100 °C for 10 min in N_2.

A solution of PCBM in chlorobenzene (20 mg/ml) was spin-coated on the $MAPbI_3$/PEDOT:PSS/ITO substrate at 1000 rpm for 30 s, followed by annealing at 110 °C for 10 min in N_2.

Finally, 0.5 nm of LiF and 100 nm of Al were subsequently deposited by thermal evaporation with a pressure of 2.4×10^{-6} Torr on top of the devices to form the back contacts. A shadow mask was used to define a 2×2 array of 0.4×0.6 cm^2 rectangular contacts. The solar cells were then encapsulated with a glass cover using an ultraviolet-curable epoxy sealant (XNR5570-A1 NAGASE ChemTex), with an ultraviolet exposure of 3 min.

2.3. Materials and Device Characterization

Absorption spectra were taken by a Jasco V670 UV-Vis-NIR spectrophotometer.

I-V measurements were performed between - 0.2 and +1.2 V, with a step size of 5 mV, using an IviumStat SourceMeter. A PEC-L01 Peccell solar simulator operating at 100 mW/cm^2 was used to simulate the solar spectrum under AM1.5G conditions. An aperture area of 0.15 cm^2 was placed over the device during *I-V* measurements.

3. Simulation Model

In this work, we used the structure ITO(160 nm)/PEDOT:PSS(40 nm)/$MAPbI_3$ (210 nm)/PCBM(50 nm)/LiF(0.5 nm)/Al(120 nm). First of all, we performed optical simulation following to method described in the previous report [8] and obtained an exciton generation profile $G(x)$ within the $MAPbI_3$ active layer, which was used as an input for the electrical simulation step using the SCAPS-1D simulation tool [9]. If there was no recombination occurring inside a solar cell at a short circuit point, all generated charge carriers would be extracted by the built-in electric field and the maximum obtainable short-circuit current density would be $J_{SC,max}=18.1674$ mA/cm^2, according to:

$$J_{SC,max}=q\int_0^d G(x)\,dx \tag{1}$$

where q is the elementary charge and d is the thickness of the $MAPbI_3$ layer.

However, in reality, the short-circuit current density is reduced due to the recombination loss of free charge carriers, which is mainly due to trap-assisted recombination in PSCs. The recombination involving defects or trap states in the band gap is called Shockley-Read-Hall (SRH), which has the following rate [10]:

$$U_{SRH}=\frac{\left(np-n_i^2\right)N_b}{\frac{p+p_t}{v_e\sigma_e}+\frac{n+n_t}{v_h\sigma_h}} \tag{2}$$

where N_b is the density of trap states at energy level E_t; v_e and v_h the mean thermal velocities of the electron and hole, respectively; σ_e and σ_h the capture cross-section of the trap for electrons and holes, respectively; n_t the electron density when $E_{F_n}=E_t$; p_t the hole density when $E_{F_p}=E_t$.

In addition to bulk defects, interface defects also play an important role in the operation of perovskite solar cells. The interface recombination flux within a very thin layer δx around the interface is [10]:

$$U_s\delta x=\frac{\left(n_s p_s-n_i^2\right)N_i}{\frac{p_s+p_t}{v_e\sigma_e}+\frac{n_s+n_t}{v_h\sigma_h}} \tag{3}$$

where N_i is the density of the interface defect, n_s and p_s, respectively is the electron and hole density at the interface.

In this work, interface defects were introduced at both interfaces: PEDOT:PSS/$MAPbI_3$ and $MAPbI_3$/PCBM. The defect density at the $MAPbI_3$/PCBM interface is supposed to be lower due to the passivation effect of fullerene-based materials on perovskite [11].

Preliminary simulations showed that the acceptor density in PEDOT:PSS, $N_A^{PEDOT:PSS}$ should be as low as 6×10^{16} cm^{-3} to obtain a comparable V_{OC} with the experimental value. Using hole mobility of 3.2×10^{-4} $cm^2\cdot V^{-1}\cdot s^{-1}$ taken from the literature [12], the conductivity of PEDOT:PSS (Clevios PVP AI 4083) is estimated to be 3.08×10^{-6} S/cm, that is two orders of magnitude lower than the reported value [13]. Other input parameters are listed in Table 1. Here the thicknesses of PEDOT:PSS, intrinsic $MAPbI_3$ (*i*-$MAPbI_3$), and PCBM were determined from the cross-sectional SEM image of an actual device. The electron affinity of PCBM was taken from [14], whereas the bandgap value of 2.1 eV was taken from the optical absorption measurement of PCBM thin film and is also consistent with other previous reports. PCBM was reported to be good electron transport material so the uniform acceptor density was set as 2×10^{18} cm^{-3}. Dielectric permittivity, bandgap, electron affinity, electron mobility, and hole mobility of $MAPbI_3$ were taken from previous reports [15-17]. The $MAPbI_3$ layer was defined as intrinsic, so both shallow acceptor and donor densities were set as low as 10^5 cm^{-3}. The doping effects were mainly caused by MA and I vacancies (bulk defects) [3, 4]. Tables 2 and 3 describe the characteristics of the bulk defects in the $MAPbI_3$ active layer and interface defects at PEDOT:PSS/$MAPbI_3$ and $MAPbI_3$/PCBM interfaces, respectively.

Table 1. General parameters used for SCAPS-1D simulations. Work functions of anode and cathode were set in flat-band condition with PEDOT:PSS and PCBM, respectively. References from which data were taken are denoted in brackets next to the numbers

Layer	PEDOT:PSS	*i*-$MAPbI_3$	PCBM
Thickness (nm)	40	210	50
Dielectric permittivity, ε_r	3	25.7 [15]	3.9
Bandgap, E_g (eV)	2.786	1.55 [16]	2.1
Electron affinity, χ (eV)	2.2	3.88 [16]	3.91 [14]
CB effective density of states, N_C (cm^{-3})	1.0×10^{20}	1.5×10^{18}	2.2×10^{19}
VB effective density of states, N_V (cm^{-3})	1.0×10^{20}	2.0×10^{18}	2.2×10^{19}
Electron mobilty, μ_e ($cm^2\cdot V^{-1}\cdot s^{-1}$)	1.0×10^{-5}	5.5 [17]	1.0×10^{-3}
Hole mobilty, μ_h ($cm^2\cdot V^{-1}\cdot s^{-1}$)	3.2×10^{-4} [12]	6.0 [17]	1.0×10^{-9}
Shallow uniform acceptor density, N_D (cm^{-3})	0	1.0×10^5	2×10^{18}
Shallow uniform donor density, N_A (cm^{-3})	6.0×10^{16}	1.0×10^5	0

Table 2. Characteristics of bulk defects in $MAPbI_3$ ALs used for SCAPS-1D simulations

Characteristics	MA vacancy (V_{MA}')	I vacancy ($V_I^{\bullet}$)
Charge type	Single acceptor (0/1–)	Single donor (0/1+)
E_b (eV) [18]	0.08 eV below E_V	0.03 eV above E_C
Energetic distribution	Gaussian with a width E_{b0} of 0.2 eV	

Table 3. Characteristics of interface defects used for SCAPS-1D simulations. σ_{ie} and σ_{ih} are capture cross-sections for electrons and holes, respectively

Interface	PEDOT:PSS/$MAPbI_3$	$MAPbI_3$/PCBM
Defect type	Donor	Acceptor
σ_{ie} (cm^2)	10^{-19}	10^{-19}
σ_{ih} (cm^2)	10^{-21}	10^{-19}
Energetic distribution	CB tail	VB tail
Energy with respect to reference, E_i (eV)	0.8 eV below E_C of $MAPbI_3$	0.8 eV above E_V of $MAPbI_3$
Characteristic energy, E_{i0} (eV)	0.1	0.1
Total density, N_{i0} (cm^{-2})	4.71×10^{11}~4.77×10^{11}	0 to 2.3×10^{12}

4. Results and Discussion

In this work, we aimed to fit *J-V* characteristics and performance parameters to the experimental data (Table 4).

Table 4. Performance parameters of an actual device measured at forward and reverse scan directions.

Scan direction	V_{OC} (V)	J_{SC} (mA/cm^2)	FF (%)	PCE (%)
Forward scan	0.92	13.66	67.0	8.42
Reverse scan	0.91	13.81	69.5	8.73

First of all, the dependence of V_{OC}, J_{SC}, and FF on defect density at the PEDOT:PSS/$MAPbI_3$ interface was investigated, as shown in Fig. 1. Interface defects deteriorate all performance parameters according to Eq. (3). In general, the recombination rate increases monotonically with the defect density, so the losses in J_{SC} also increase with defect density (see Fig. 2). However, the dependence is nonlinear because in Eq. (3), the recombination rate depends not only on N_i, but also on charge carrier density n_s and p_s. In addition, although simulations in Figs. 1 and 2 were performed at a fixed value of bulk defect density N_b, the increase of loss in J_{SC} was observed not only at the interface ($J_{loss\text{-}interface}$), but also in the bulk ($J_{loss\text{-}bulk}$) as N_i increased. This indicates the strong correlation between bulk and interface defects because both recombination rates depend on the charge carrier densities, while charge carrier densities in their turns depend on photogeneration and recombination events. The *J-V* characteristics of solar cells can be described by the following Shockley equation:

$$J = -J_L + J_0 \exp\left(\frac{V - JR_s}{\eta\left(k_B T/q\right)}\right) + \frac{V - JR_s}{R_{sh}} \quad (4)$$

with J_L is the photocurrent, J_0 the reverse saturation current density, η the ideality factor, R_s and R_{sh} the parasitic series and shunt (parallel) resistances, respectively. In an ideal case without R_s and R_{sh}, V_{OC} depends on J_L as following:

$$V_{OC} = \frac{\eta k_B T}{e} \ln\left(\frac{J_L}{J_0}\right) \quad (5)$$

By fitting simulated *J-V* curves to the Shockley equation (4), we can see the increasing trend of both η and J_0 as N_{i1} increases (Table 5). However, the reduction of J_L/J_0 is more substantial than the increase of η, which leads to an overall decrease in V_{OC}. Finally, the decline of FF is caused mainly by the increase of both (η, J_0), and the severe reduction of R_{sh} as N_{i1} increases.

Table 5. Performance parameters and parameters obtained by fitting the simulated *J-V* characteristics to Shockley equation (4) at various values of N_{i1}

N_{i1} (cm^{-2})	V_{OC} (V)	J_{SC} (mA/cm^2)	FF (%)	PCE (%)	R_s ($\Omega \cdot cm^2$)	R_{sh} ($\Omega \cdot cm^2$)	J_L (mA/cm^2)	η	J_0 (A/cm^2)
5×10^{10}	0.95	16.77	76.72	12.22	4.4	2199.5	16.81	1.25	2.75×10^{-15}
10^{11}	0.942	16.27	75.53	11.58	4.33	1523.8	16.33	1.3	1.19×10^{-14}
2×10^{11}	0.934	15.61	73.56	10.73	4.22	1027.6	15.69	1.42	1.29×10^{-13}
5×10^{11}	0.925	14.31	69.23	9.16	3.92	613.4	14.42	1.7	9.29×10^{-12}
10^{12}	0.917	12.88	64.38	7.61	3.51	435	13	2.01	2.27×10^{-10}
2×10^{12}	0.91	10.95	58.41	5.82	2.93	336.8	11.05	2.31	2.02×10^{-9}

Interpolations of curves in Fig. 1 to experimental values of V_{OC}, J_{SC}, and FF give different values of $N_{i1}^{PEDOT:PSS/MAPbI_3}$: 1.956×10^{12} cm^{-2}, 6.753×10^{11} cm^{-2}, and 4.812×10^{11} cm^{-2}, respectively. Therefore, the variation of $N_{i1}^{PEDOT:PSS/MAPbI_3}$ is not sufficient for fitting all three performance parameters.

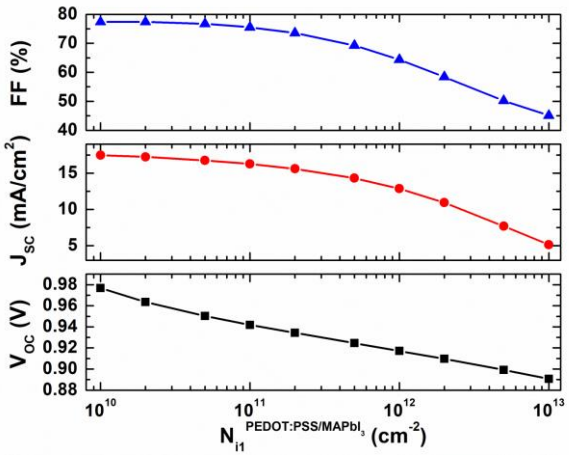

Figure 1. The dependence of performance parameters (V_{OC}, J_{SC}, and FF) on the interface defect density at the PEDOT:PSS/$MAPbI_3$ interface, $N_{i1}^{PEDOT:PSS/MAPbI_3}$. In these simulations, the following parameters were used: $E_g^{PEDOT:PSS} = 2.8$ eV, $N_A^{PEDOT:PSS} = 6\times10^{16}$ cm^{-3}, $N_b^{MAPbI_3} = 5\times10^{15}$ cm^{-3}, $N_{i2}^{MAPbI_3/PCBM} = 5\times10^{10}$ cm^{-2}.

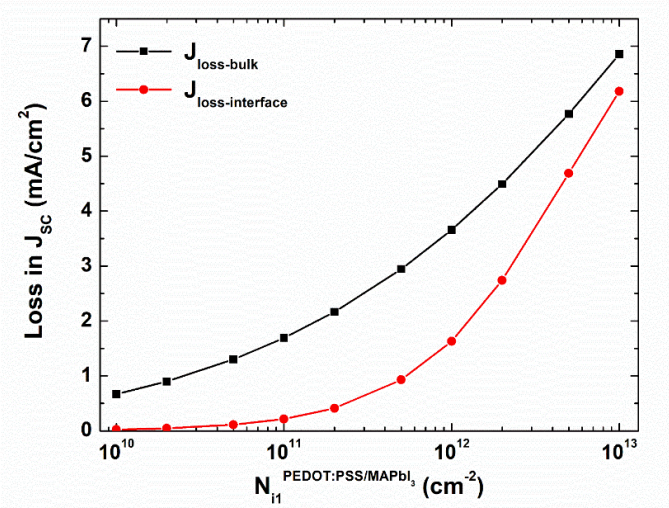

Figure 2. The dependence of loss in J_{SC} due to recombination at the bulk and interface defects. Data were extracted from simulations corresponding to Fig. 1.

In the next simulations, we decided to use $N_{i1}^{PEDOT:PSS/MAPbI_3} = 5\times10^{11}$ cm^{-2} and other parameters as fixed values, while the density of intrinsic defect (bulk defect) in the $MAPbI_3$ active layer, $N_b^{MAPbI_3}$ was allowed to vary between 5×10^{13} and 5×10^{17} cm^{-3}. As shown in Fig. 3, V_{OC} and J_{SC} start to exhibit significant reduction as $N_b^{MAPbI_3}$ reaches 5×10^{15} cm^{-3}. To obtain a comparable J_{SC} with the experimental value, we used bulk defect density $N_b^{MAPbI_3} = 6.116\times10^{15}$ cm^{-3} in the next simulations.

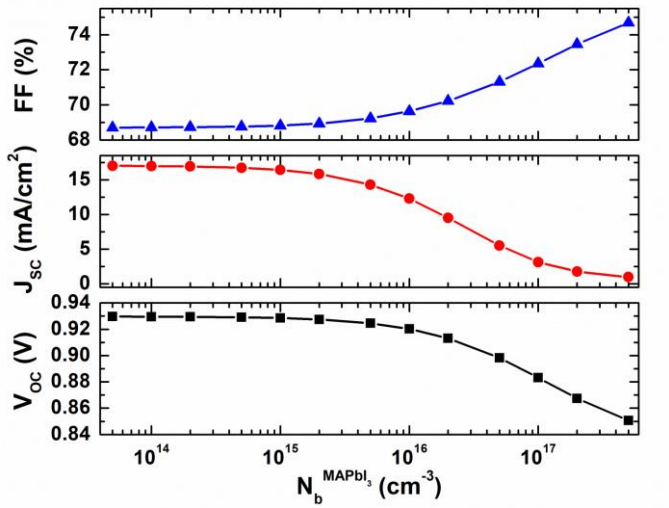

Figure 3. The dependence of performance parameters (V_{OC}, J_{SC}, and FF) on the intrinsic defect (V_{MA}' and $V_I^{\bullet}$) density in $MAPbI_3$, $N_b^{MAPbI_3}$. In these simulations, the following parameters were used: $E_g^{PEDOT:PSS} = 2.8$ eV, $N_A^{PEDOT:PSS} = 6\times10^{16}$ cm^{-3}, $N_{i1}^{PEDOT:PSS/MAPbI_3} = 5\times10^{11}$ cm^{-2}, $N_{i2}^{MAPbI_3/PCBM} = 5\times10^{10}$ cm^{-2}.

Using the above-mentioned value of $N_b^{MAPbI_3}$, we performed simulations as the bandgap of PEDOT:PSS, $E_g^{PEDOT:PSS}$ varied from 2.75 to 2.85 eV (Fig. 4). As $E_g^{PEDOT:PSS}$ varies, the band offset between PEDOT:PSS and $MAPbI_3$ changes and affects the hole extraction efficiency at the anode side. As a result, in the above-mentioned varying range $E_g^{PEDOT:PSS}$, all performance parameters show a linear dependence on $E_g^{PEDOT:PSS}$ as follows:

$$eV_{OC}(\text{eV}) = E_g - 1.876 \quad (4)$$

$$J_{SC}(\text{mA/cm}^2) = 11.2772 + 0.90425 \times E_g \quad (5)$$

$$\text{FF}(\%) = 35.06611 + 12.22727 \times E_g \quad (6)$$

Equation (4) provides an optimal value of $E_g^{PEDOT:PSS} = 2.786$ eV to get V_{OC} of 0.91 V. This value was used for the next simulations, when J_{SC} and FF were fitted simultaneously to experimental values.

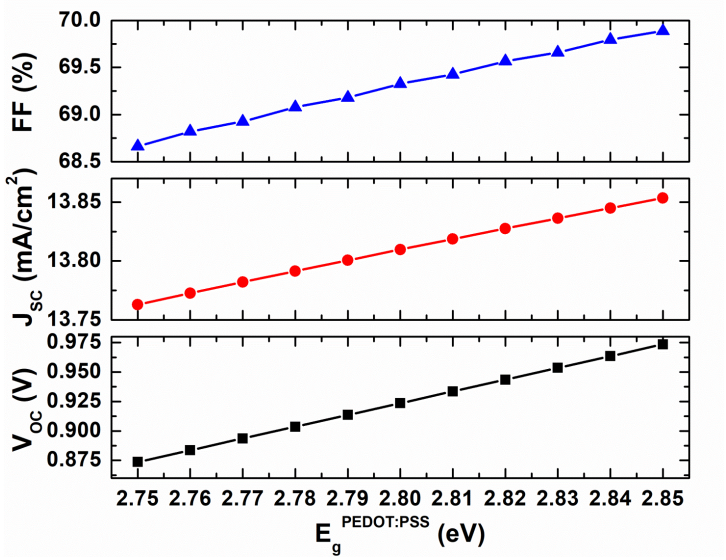

Figure 4. The dependence of performance parameters (V_{OC}, J_{SC}, and FF) on the bandgap of PEDOT:PSS, $E_g^{PEDOT:PSS}$. In these simulations, the following parameters were used: $N_A^{PEDOT:PSS} = 6\times10^{16}$ cm^{-3}, $N_{i1}^{PEDOT:PSS/MAPbI_3} = 5\times10^{11}$ cm^{-2}, $N_b^{MAPbI_3} = 6.116\times10^{15}$ cm^{-3}. $N_{i2}^{MAPbI_3/PCBM} = 5\times10^{10}$ cm^{-2}.

To fit experimental results, there is a way to vary simultaneously two input parameters, and $N_{i1}^{PEDOT:PSS/MAPbI_3}$ and $N_b^{MAPbI_3}$ were chosen in this step. Figures 5a, 5b show the influence of $N_{i1}^{PEDOT:PSS/MAPbI_3}$ and $N_b^{MAPbI_3}$ on J_{SC} and FF, while $N_{i2}^{MAPbI_3/PCBM}$ was fixed at 5×10^{10} cm^{-2}. In general, both J_{SC} and FF vary linearly with defect density. In Fig. 5a, interface defects and bulk defects contribute equally to the reduction of J_{SC}, while in Fig. 5b, interface defects are the main reason for the reduction of FF. Contour lines corresponding to experimental values $J_{SC} = 13.811$ mA/cm^2 and FF = 69.5% are plotted in Fig. 4c. The intersection of the two lines provides the following defect density: $N_{i1}^{PEDOT:PSS/MAPbI_3} = 4.714\times10^{11}$ cm^{-2} and $N_b^{MAPbI_3} = 6.335\times10^{15}$ cm^{-3}. Using those input parameters, the

following simulated performance parameters were found: $V_{OC} = 0.91033$ V, $J_{SC} = 13.81065$ mA/cm^2, and FF = 69.5213%, which are in perfect agreement with the experimental values listed in Table 1.

It is important to note that the problem we stated in this work has multiple solutions, *i.e.* there are many sets of input parameters that all give correct values of V_{OC}, J_{SC}, and FF simultaneously. However, at each value of $N_{i2}^{MAPbI_3/PCBM}$, only one set of $N_{i1}^{PEDOT:PSS/MAPbI_3}$ and $N_b^{MAPbI_3}$ exists to meet the above requirement. We performed simulations at several values of $N_{i2}^{MAPbI_3/PCBM}$ ranging from 0 to 2.3×10^{12} cm^{-2}, and the variations of optimal $N_{i1}^{PEDOT:PSS/MAPbI_3}$ and $N_b^{MAPbI_3}$ on $N_{i2}^{MAPbI_3/PCBM}$ are shown in Fig. 5. As $N_{i2}^{MAPbI_3/PCBM}$ exceeds 2.3×10^{12} cm^{-2}, the simulations cannot be performed due to convergence failure at short-circuit point. As shown in Fig. 5, $N_{i1}^{PEDOT:PSS/MAPbI_3}$ varies in a very narrow range from 4.712×10^{11} to 4.767×10^{11} cm^{-2}, and tends to saturate to those values as $N_{i2}^{MAPbI_3/PCBM}$ smaller than 0.6×10^{12} cm^{-2} and larger than 1.2×10^{12} cm^{-2}, respectively. In contrast, $N_b^{MAPbI_3}$ decreases monotonically as $N_{i2}^{MAPbI_3/PCBM}$ increases, and also tends to saturate at high $N_{i2}^{MAPbI_3/PCBM}$.

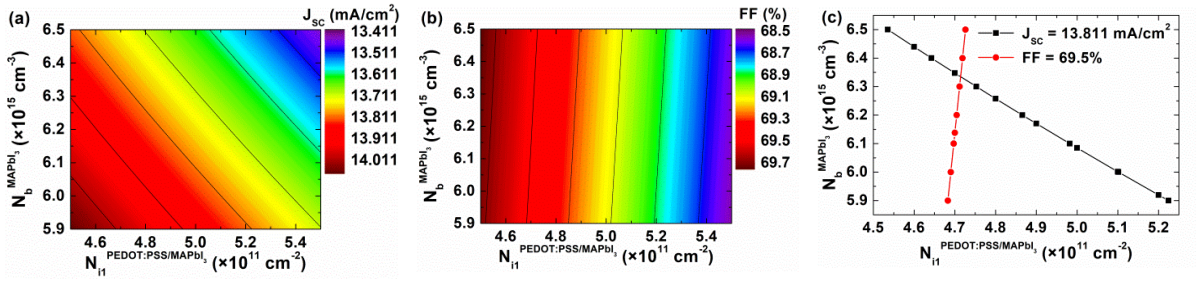

Figure 5. (a, b) Contour plots showing the influence of $N_{i1}^{PEDOT:PSS/MAPbI_3}$ and $N_b^{MAPbI_3}$ on J_{SC} and FF. In these simulations, the following parameters were used: $E_g^{PEDOT:PSS} = 2.786$ eV, $N_A^{PEDOT:PSS} = 6\times10^{16}$ cm^{-3}, $N_{i2}^{MAPbI_3/PCBM} = 5\times10^{10}$ cm^{-2}; (c) Contour lines corresponding to $J_{SC} = 13.811$ mA/cm^2 and FF = 69.5%.

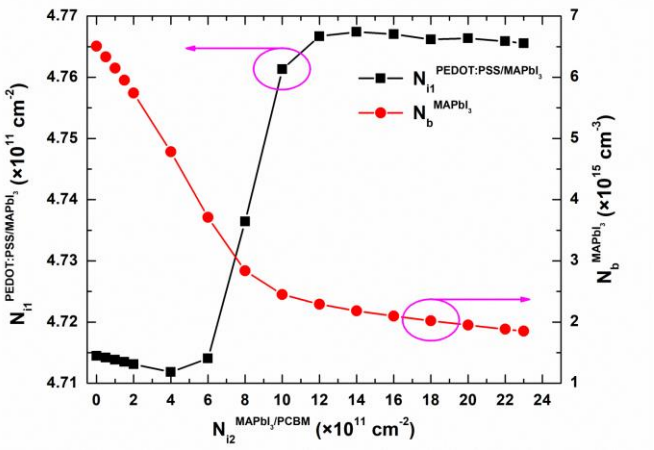

Figure 6. Variation of $N_{i1}^{PEDOT:PSS/MAPbI_3}$ and $N_b^{MAPbI_3}$ with $N_{i2}^{MAPbI_3/PCBM}$ as results of fitting simultaneously J_{SC} and FF to experimental data.

Experimental *J-V* curve and simulated *J-V* curves at two typical values of $N_{i2}^{MAPbI_3/PCBM}$ are presented in Fig. 7a. Obviously, under illumination, simulated curves are identical to the experimental curve. In contrast, there is a mismatch in dark current density between simulated and experimental curves at applied voltage larger than V_{OC}, whereas the two simulated curves are identical. In addition, there is a crossover between the illuminated and dark experimental *J-V* curves, whereas this phenomenon is not observed in simulated curves. The crossover phenomenon was observed mainly in thin-film solar cells including chalcogenide solar cells, and organic solar cells. One main reason was addressed in [19], which showed that a low contact-to-contact built-in potential can produce a voltage-dependent photocurrent that leads to *J-V* crossover at a voltage that is almost exactly the device's built-in potential. In our simulation model, the voltage-dependent photocurrent was not considered, hence the *J-V* crossover was not observed in the simulated *J-V* curve.

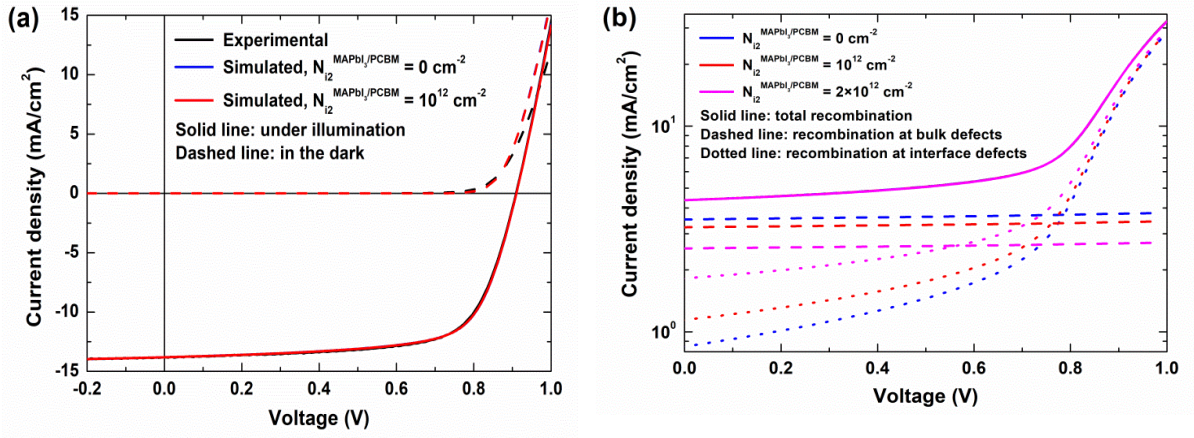

Figure 7. (a) Experimental *J-V* curve and simulated *J-V* curves at two typical values of $N_{i2}^{MAPbI_3/PCBM}$; (b) Simulated recombination currents at different values of $N_{i2}^{MAPbI_3/PCBM}$.

As seen in Fig. 7b, the recombination current densities at bulk defects are constant at all values of applied voltage, while recombination current densities at interface defects and total recombination current densities increase with the rising of applied bias. It is also reasonable that at all applied voltages, the current loss at interface defect increases, while the current loss at bulk defect reduces as $N_{i2}^{MAPbI_3/PCBM}$ increases from 0 to 2.3×10^{12} cm^{-2}.

The real short-circuit current density can be obtained by the following relation:

$$J_{SC,real} = J_{SC,max} - J_{bulk\ recombination} - J_{interface\ recombination} \quad (7)$$

Here, $J_{bulk\ recombination}$ and $J_{interface\ recombination}$ are recombination current densities at bulk and interface defects, respectively. It is important to note that the current losses at each interface were not distinguished in the calculation of $J_{interface\ recombination}$.

As listed in Table 6, the current loss due to bulk recombination is largest at 3.51927 (mA/cm^2) as $N_b^{MAPbI_3} = 6.509\times10^{15}$ (cm^{-3}) and $N_{i2}^{MAPbI_3/PCBM} = 0$ cm^{-2}.

Table 6. Components of recombination current density at different densities of bulk and interface defects at short-circuit condition ($V = 0$ V)

$N_{i2}^{MAPbI_3/PCBM}$ (cm^{-2})	$N_{i1}^{PEDOT:PSS/MAPbI_3}$ (cm^{-2})	$N_b^{MAPbI_3}$ (cm^{-3})	$J_{total\ recombination}$ (mA/cm^2)	$J_{bulk\ recombination}$ (mA/cm^2)	$J_{interface\ recombination}$ (mA/cm^2)
0	4.714×10^{11}	6.509×10^{15}	4.36788	3.51927	0.84861
10^{12}	4.761×10^{11}	2.451×10^{15}	4.36757	3.22501	1.14257
2×10^{12}	4.766×10^{11}	1.950×10^{15}	4.36545	2.54548	1.81997

5. Conclusions

In this work, we have developed a method of determination of bulk and interface defects by combining experimental *J-V* data and the SCAPS-1D simulation tool. Based on the simulation results, as the density of interface defect at $MAPbI_3$/PCBM interface increases in a wide range from 0 to 2.3×10^{12} cm^{-2}, the density of interface defect at PEDOT:PSS/$MAPbI_3$ varies insignificantly between 4.71×10^{11} cm^{-2} and 4.77×10^{11} cm^{-2}. Although this method can only bring multiple sets of defect density in the current device structure for a unique *J-V* characteristic, it will be helpful if one can use some additional experimental techniques that can exactly identify the defect density at PEDOT:PSS/$MAPbI_3$ or $MAPbI_3$/PCBM interfaces.

Acknowledgements

This research is funded by Vietnam National Foundation for Science and Technology Development (NAFOSTED) under grant number 103.02-2018.55.

References

[1] H. Min, D. Y. Lee, J. Kim, G. Kim, K. S. Lee, J. Kim, M. J. Paik, Y. K. Kim, K. S. Kim, M. G. Kim, T. J. Shin, S. I. Seok, Perovskite Solar Cells with Atomically Coherent Interlayers on SnO_2 Electrodes, Nature, Vol. 598, 2021, pp. 444-450, https://doi.org/10.1038/s41586-021-03964-8.

[2] J. S. Manser, P. V. Kamat, Band Filling with Free Charge Carriers in Organometal Halide Perovskites, Nat. Photonics, Vol. 8, 2014, pp. 737-743, https://doi.org/ 10.1038/nphoton.2014.171.

[3] W. J. Yin, T. Shi, Y. Yan, Unusual Defect Physics in $CH_3NH_3PbI_3$ Perovskite Solar Cell Absorber, Appl. Phys. Lett., Vol. 104, 2014, pp. 063903, https://doi.org/10.1063/1.4864778.

[4] J. Kim, S. H. Lee, J. H. Lee, K. H. Hong, The Role of Intrinsic Defects in Methylammonium Lead Iodide, J. Phys. Chem. Lett., Vol. 5, 2014, pp. 1312-1317, https://doi.org/10.1021/jz500370k.

[5] M. H. Du, Efficient Carrier Transport in Halide Perovskites: Theoretical Perspectives, J. Mater. Chem. A, Vol. 2, 2014, pp. 9091-9098, https://doi.org/10.1039/c4ta01198h.

[6] D. Yang, W. Ming, H. Shi, L. Zhang, M. H. Du, Fast Diffusion of Native Defects and Impurities in Perovskite Solar Cell Material $CH_3NH_3PbI_3$, Chem. Mater., Vol. 28, No 12, 2016, pp. 4349-4357, https://doi.org/10.1021/acs.chemmater.6b01348.

[7] Q. Wang, Y. Shao, H. Xie, L. Lyu, X. Liu, Y. Gao, J. Huang, Qualifying Composition Dependent *p* and *n* Self-doping in $CH_3NH_3PbI_3$, Appl. Phys. Lett., Vol. 105, 2014, pp. 163508, https://doi.org/ 10.1063/1.4899051.

[8] N. D. Cuong, Optical Simulation of Planar $CH_3NH_3PbI_3$ Perovskite Solar Cells, VNU J. Sci. Math. Phys, Vol. 35, No. 3, 2019, pp. 98-106, https://doi.org/10.25073/2588-1124/vnumap.4349.

[9] A. Niemegeers, M. Burgelman, K. Decock, S. Degrave, V. Johan, SCAPS (a Solar Cell Capacitance Simulator). Available online: http://scaps.elis.ugent.be/SCAPSinstallatie.html (accessed om: February 25th, 2019).

[10] J. Nelson, The Physics of Solar Cells, Imperial College Press, 2003, pp. 106-112.

[11] Y. Shao, Z. Xiao, C. Bi, Y. Yuan, J. Huang, Origin and Elimination of Photocurrent Hysteresis by Fullerene Passivation in $CH_3NH_3PbI_3$ Planar Heterojunction Solar Cells, Nat. Commun., Vol. 5, 5784, 2014, pp. 1-7, http://doi.org/10.1038/ncomms6784.

[12] C. C. Chang, J. H. Tao, C. E. Tsai, Y. J. Cheng, C. S. Hsu, Cross-linked Triarylamine-Based Hole-Transporting Layer for Solution-Processed PEDOT:PSS-Free Inverted Perovskite Solar Cells, ACS Appl. Mater. & Interfaces, Vol. 10, No. 25, 2018, pp. 21466-21471, http://doi.org/10.1021/acsami.8b04396.

[13] Y. Yang, H. Deng, Q. Fu, Recent Progress on PEDOT:PSS Based Polymer Blends and Composites for Flexible Electronics and Thermoelectric Devices, Mater. Chem. Front., Vol. 4, No. 11, 2020, pp. 3130-3152, http://doi.org/10.1039/d0qm00308e.

[14] Y. He, H. Y. Chen, J. Hou, Y. Li, Indene - C60 Bisadduct: A New Acceptor for High-Performance Polymer Solar Cells, Journal of the American Chemical Society, Vol. 132, 2010, pp. 1377-1382, https://doi.org/10.1021/ja908602j.

[15] F. Brivio, A. B. Walker, A. Walsh, Structural and Electronic Properties of Hybrid Perovskites for High-Efficiency Thin-Film Photovoltaics from First-Principles, APL Mater. Vol. 1, No. 4, 2013, pp. 2011-2016, https://doi.org/10.1063/1.4824147.

[16] H. S. Jung, N. G. Park, Perovskite Solar Cells: From Materials to Devices, small, Vol. 11, No. 1, 2015, pp. 10-25, https://doi.org/10.1002/smll.201402767.

[17] C. Motta, F. El-Mellouhi, S. Sanvito, Charge Carrier Mobility in Hybrid Halide Perovskites, Sci. Rep., Vol. 5, 2015, pp. 1-8, https://doi.org/10.1038/srep12746.

[18] W. J. Yin, T. Shi, Y. Yan, Unique Properties of Halide Perovskites as Possible Origins of the Superior Solar Cell Performance, Adv. Mater., Vol. 26, No. 27, 2014, pp. 4653-4658, http://doi.org/10.1002/adma.201306281.

[19] J. E. Moore, S. Dongaonkar, R. V. K. Chavali, M. A. Alam, M. S. Lundstrom, Correlation of Built-in Potential and *I-V* Crossover in Thin-Film Solar Cells, IEEE J. Photovoltaics, Vol. 4, No. 4, 2014, pp. 1138-1148, http://doi.org/10.1109/JPHOTOV.2014.2316364.